

ManifoldPlus: A Robust and Scalable Watertight Manifold Surface Generation Method for Triangle Soups

JINGWEI HUANG, Stanford University
 YICHAO ZHOU, University of California, Berkeley
 LEONIDAS GUIBAS, Stanford University

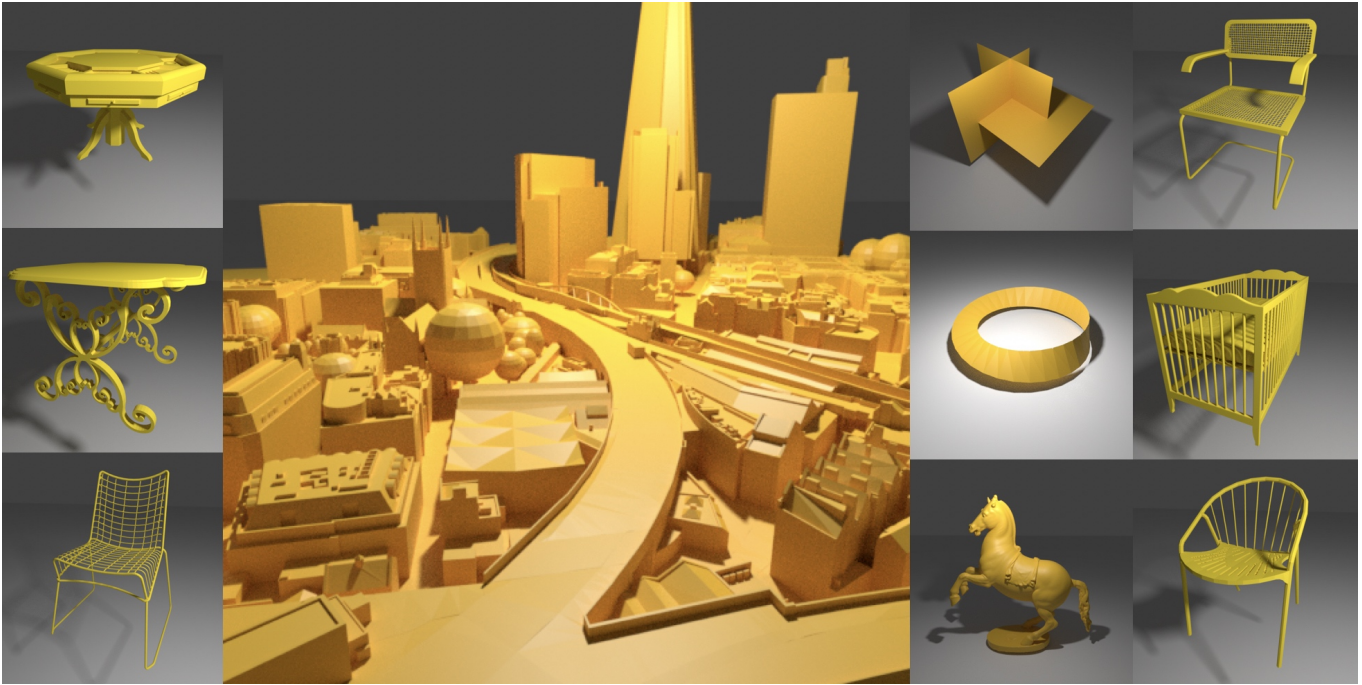


Fig. 1. ManifoldPlus: We present a method to robustly convert complex meshes in target scale to watertight manifolds.

We present ManifoldPlus, a method for robust and scalable conversion of triangle soups to watertight manifolds. While many algorithms in computer graphics require the input mesh to be a watertight manifold, in practice many meshes designed by artists are often for visualization purposes, and thus have non-manifold structures such as incorrect connectivity, ambiguous face orientation, double surfaces, open boundaries, self-intersections, etc. Existing methods suffer from problems in the inputs with face orientation and zero-volume structures. Additionally most methods do not scale to meshes of high complexity. In this paper, we propose a method that extracts exterior faces between occupied voxels and empty voxels, and uses a projection-based optimization method to accurately recover a watertight manifold that resembles the reference mesh. Compared to previous methods, our methodology is simpler. It does not rely on face normals of the input triangle soups and can accurately recover zero-volume structures. Our algorithm is scalable, because it employs an adaptive Gauss-Seidel method for shape optimization, in which each step is an easy-to-solve convex problem. We

Authors' addresses: Jingwei Huang, Stanford University; Yichao Zhou, University of California, Berkeley; Leonidas Guibas, Stanford University.

test ManifoldPlus on ModelNet10 [Wu et al. 2015] and AccuCity¹ datasets to verify that our methods can generate watertight meshes ranging from object-level shapes to city-level models. Furthermore, through our experimental evaluations, we show that our method is more robust, efficient and accurate than the state-of-the-art. Our implementation is publicly available².

CCS Concepts: • **Computing methodologies** → *Mesh geometry models*.

Additional Key Words and Phrases: Manifold, Meshing

Jingwei Huang, Yichao Zhou, and Leonidas Guibas. Arxiv 2020. ManifoldPlus: A Robust and Scalable Watertight Manifold Surface Generation Method for Triangle Soups

1 INTRODUCTION

Watertight manifolds are ubiquitous in computer graphics. They are usually represented as *orientable 2-manifold* triangle meshes. Such topology gives a convenient surface representation of objects where local geodesic neighborhoods can be consistently analyzed. Various tasks in computer graphics often mandate or at least prefer a watertight manifold mesh as input, including geometry-based

¹<https://www.accucities.com>

²<https://github.com/hjwdzh/ManifoldPlus>

segmentation [Gelfand and Guibas 2004; Kim 1992], quadrangulation [Huang et al. 2018b; Jakob et al. 2015], UV mapping [Burley and Lacewell 2008; Poranne et al. 2017], mesh deformation [Sorkine and Alexa 2007; Uy et al. 2020], physically-based simulation [Baraff and Witkin 1998; Wu et al. 2001], finite element analysis [Zienkiewicz et al. 1977], surface feature extraction for machine learning [Huang et al. 2019; Masci et al. 2015], and so forth. Since 3D data is usually acquired as human-designed CAD models and scans, manifold conversion from these data is an important problem. However, these data is challenging to handle, especially because of the existence of sharp features, zero-volume structures (e.g. ShapeNet [Chang et al. 2015]), and unavailability of correct exterior information (e.g. surface normal), which prevents existing methods from robustly producing high-quality watertight manifolds. For example, the famous marching cubes algorithm [Lorensen and Cline 1987] requires exterior information to distinguish positive (exterior) from negative (interior) distances for zero-contour extraction based on a signed distance field. However, there is no association of signs that successfully enables marching cubes to construct both the orange and green faces at the T-junction example shown in Figure 2(a). Furthermore, the precision of marching cubes is only up to the side length of voxels, which makes it hard to preserve sharp features or sub-voxel structures in the final mesh. Delaunay triangulation-based methods suffer from similar issues: To perfectly recover the geometry, both sides of the green edge in Figure 2(b) should be considered as exterior while only one side of the orange edge should be considered exterior. This natural ambiguity of exterior information is challenging to remove. Even with perfect exterior information, surface extraction step [Boissonnat 1984] needs to keep some exterior volumes to avoid non-manifold edges at the T-junction (marked as the red spot) in Figure 2(b).

In this work, we target the problem of resolving exterior ambiguity and zero-volume structures and of obtaining a manifold that accurately resembles the input triangle soup. As shown in Figure 2(c), we build an octree volume where regions surrounding the reference mesh are split into leaf nodes as voxels with a fine resolution. Instead of determining signed distances for these voxels and performing marching cubes, we simply mark voxels as occupied if they intersect the reference mesh. Then, we determine exterior nodes as those who are connected to the boundary of the volume, without passing any occupied voxels. We extract surfaces between exterior and occupied nodes to guarantee that generated surfaces are manifolds while preserving zero-volume structures. There are two main advantages to this simple solution: First, our method does not rely on the normal direction of faces in input meshes to decide exterior, as we can directly test whether one side of the face is connected to the exterior volume boundary. Second, we can preserve sub-voxel and zero-volume structures, as shown in Figure 2(c).

However, the vertices and faces on the extracted manifold with the aforementioned pipeline are always on the voxel grid, and cannot approximate the reference mesh geometry well. Therefore, we project extracted vertices to the nearest positions in the reference mesh (blue arrows in Figure 2(c)). However, doing this in a brute force way might cause problematic triangle inversions. Our key technical contribution here is to formulate the projection as an energy minimization problem with inversion-free constraints and use

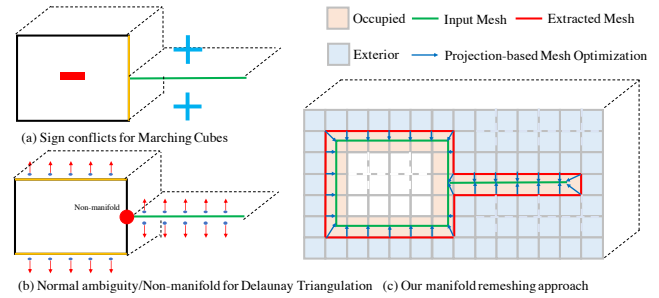


Fig. 2. Illustration of manifold remeshing challenge. (a) Marching cubes cannot resolve sign conflicts at T-junctions. (b) There is natural ambiguity regarding exterior information. Non-manifold edges can be created at T-junctions by removing all exterior regions. (c) Our novel method addresses these problems.

a Gauss-Seidel strategy to solve the optimization efficiently. Typically, a triangle inversion means that the triangle orientation is inconsistent with the orientation of its local neighborhood. Therefore, we can use vertex normal to describe the local orientation and detect triangle inversion if the dot product between the triangle normal and any of its vertices' normals is negative. Based on this observation, we propose to introduce three hard constraints for each triangle between its face normal and three vertex normals and optimize not only for vertex positions but also for vertex normals. Since we want vertex positions to be close to the reference mesh and vertex normals to best describe local orientation, we design our energy as the sum of distances between vertices to the reference mesh and distances between vertex normals to the area-based interpolation of its incident face normals. We observe that by solving for each variable while fixing all other variables, our proposed problem becomes convex. Therefore, we apply a Gauss-Seidel scheme and iteratively update each variable. Empirically, we find that the optimization converges with a small constant number of iterations. With additional sharp-preserving processing, we can detect and keep sharp features from the reference mesh.

We implement this algorithm and evaluate its performance based on several criteria. For correctness, we verify whether our extracted mesh is topologically a watertight manifold and satisfies the inversion free condition. For efficiency, we report the processing time for different complexity of input meshes. For accuracy, we report the maximum and mean distance between vertices on the extracted mesh and the reference mesh. Compared to previous state-of-the-art methods, ours is the only method that converts mesh to a watertight manifold correctly and efficiently with detailed feature preservation. We demonstrate that our algorithm can handle zero-volume structures with a lot of self-intersections, organic shapes, and extremely complex meshes on a city scale. Finally, with a small modification, our method can be used for a standard surface reconstruction purpose for scanning data. In summary, our main contributions are:

- Propose a novel surface extraction scheme that handles exterior ambiguity and zero-volume structures.
- Give a new formulation for mesh vertices projection optimization with triangle inversion-free constraints.

- Implement a robust and accurate software with thorough evaluations on large-scale datasets, with additional sharp-preservation features.
- Demonstrate our capability to handle complex meshes in large-scale and scanning data.

2 RELATED WORK

According to [Attene et al. 2013], existing methods can be classified as volumetric surface remeshing and direct local mesh repairing. Volumetric methods first convert the input triangle mesh into a volumetric representation surrounding the reference mesh, e.g., a sign distance field on voxels, and then reconstruct the manifold output from this volumetric representation using a contour extraction algorithm. In this section, we discuss several popular volumetric representations, highlight our key difference from these methods in modeling the zero-contour, and briefly discuss local mesh repairing methods. Finally, we compare our mesh projection process with other shape registration methods.

Volumetric Representation. Typical volumetric representations include regular grid [Curless and Levoy 1996; Nooruddin and Turk 2003] optionally accelerated with octrees [Agarwala 2007; Calakli and Taubin 2011; Hornung and Kobbelt 2006; Ju 2004; Kazhdan et al. 2006; Kazhdan and Hoppe 2013], polyhedron from Delaunay triangulation [Boissonnat 1984; Chew 1989; Hu et al. 2018; Rineau and Yvinec 2007; Shewchuk 2002] or BSP trees [Murali and Funkhouser 1997]. Although a polyhedron is better than a regular grid at keeping the exact input geometry, the constrained Delaunay triangulation is hard to implement to correctly handle all degenerate cases, e.g., non-zero volume structures, according to [Attene 2018]. Furthermore, it takes a long time to subdivide the original mesh to avoid self-intersections as exact construction is required for robustness. Therefore, we choose the regular grid as our representation since it is easy to implement and does not suffer from precision or self-intersection problems, which makes it usually more scalable and robust. Although surface extracted from regular grids using marching cubes [Chernyaev 1995; Doi and Koide 1991; Dürst 1988; Lorensen and Cline 1987] is not precise, we do not suffer from this issue since our newly proposed projection optimization moves extracted vertices precisely to the reference mesh.

Zero-contour Extraction. Zero-contour is commonly modeled with the help of a signed distance field. The sign of the distance is usually determined given surface normal [Agarwala 2007; Calakli and Taubin 2011; Kazhdan et al. 2006; Kazhdan and Hoppe 2013], scanning sensor location [Curless and Levoy 1996; Newcombe et al. 2011], or geometry heuristics [Boissonnat 1984; Hornung and Kobbelt 2006]. One of the most geometrically meaningful and robust solutions is presented in [Ju 2004] where positive signs are determined by computing an occupancy grid and detecting exterior regions with a broad-first search from the volume boundary. Unfortunately, the aforementioned representations fail to model zero-volume structure as zero-contour since grids from both sides are associated with a positive sign. Instead, we do not compute the continuous signed distance for grid positions, but simply determine voxel status as

occupied, exterior, or interior based on the occupancy grid. Zero-volume structures are therefore extracted as surfaces shared by occupied and exterior voxels. Further, while zero-contour determined by distance field with linear interpolation is inaccurate, our mesh projection optimization guarantees the accuracy in our final results.

Local Mesh Repairing. These methods directly operate on the input mesh to avoid unnecessary change. A typical workflow is to address self-intersections by subdivisions [Attene 2014] with hybrid geometric kernel [Attene 2017], remove non-manifold elements by singular vertex and edge decomposition [Guéziec et al. 2001; Rossignac and Cardoze 1999] and greedily pair boundaries together. MeshFix [Attene 2010] works on solid objects and address problematic local regions. An integer optimization based on visual cues [Chu et al. 2019] can be introduced to achieve a more global mesh repairing strategy. Among them, MeshFix [Attene 2010] does not handle zero-volume structure. Other repairing methods can generate boundary edges during decomposition at T-junctions. These additional boundary edges are not ideal for geodesic analysis-related applications. As we test, [Attene 2018] is quite robust for extracting high-quality watertight manifold by computing the outer hull. However, it introduces additional thickness for zero-volume structures and causes non-manifold issues in 0.8% among our test shapes. Additionally, massive computation of self-intersections and triangulation makes this method less efficient. Comparing with mesh repairing methods, our method is efficient and robust and always guarantees a watertight manifold result.

Shape Registration. Our key challenge is to project our extracted mesh to the reference mesh. One related and widely researched problem is called shape registration, in which scenario a transformation function is optimized to register the source shape to the target using the iterative-closest-point (ICP) algorithm [Besl and McKay 1992; Chen and Medioni 1992]. The transformation can be rigid [Diez et al. 2015; Rusinkiewicz and Levoy 2001] or nonrigid [Li et al. 2008; Newcombe et al. 2015; Sumner et al. 2007], and non-rigid ICP usually comprises a rigidity regularization applied to the source mesh preserving local geometry features. Although we are handling the shape registration problem, we target at fixing the local geometry of our extracted mesh rather than preserving it. Therefore, common regularization energy does not apply. We propose to introduce hard inversion-free constraints rather than soft energy constraints for regularization. This gives maximum freedom for vertices to move within the constraints so that a nearly perfect fitting is possible. Although hard constraints introduce additional complexity, we derive a Gauss-Seidel optimization strategy to effectively solve this problem.

3 APPROACH

In this section, we discuss the details of our manifold conversion algorithm. Our input is a reference triangle mesh $\mathcal{M}_r = \{\mathcal{V}_r, \mathcal{F}_r\}$ with a set of vertices \mathcal{V}_r and a set of triangles represented as vertex indices \mathcal{F}_r . We discuss surface extraction in Section 3.1, manifold optimization formulation in Section 3.2, our Gauss-Seidel solver in Section 3.3, and sharp preservation processing in Section 3.4.

3.1 Surface Extraction

We begin by constructing a set of voxels from \mathcal{M}_r (e.g. orange voxels in Figure 2(c)) at a user-specified resolution using an octree representation. First, we normalize the reference mesh by re-centering it to the origin and applying a uniform scale so that all the absolute values of vertex coordinates are smaller than 1. Next, we build the occupancy grid on octree with volume ranging from -1.1 to 1.1 . We assign the entire face set \mathcal{F}_r to the root since it guarantees to contain the whole reference mesh. Then, we recursively split the octree until a certain node is not intersected by any triangles, or the maximum tree depth H (specified by the user) is achieved. We mark nodes as occupied or empty depending on whether it intersects with any triangles. The overall time complexity for our octree construction is $O(|\mathcal{F}_r| \cdot H)$. The pseudo-code for building the octree can be found at Appendix A.

After we construct the octree, we build connections between all neighboring nodes that share faces. Since each node corresponds to a cube with six faces, we split neighbors into six connection groups, each of which corresponds to one of the node's faces. Note that each group may have multiple neighbors since neighboring octree nodes can have different resolutions. The pseudo-code of connection construction can be found at Appendix B.

Boundary nodes can be easily detected as those with boundary faces whose corresponding connection groups have no neighbors. Then, we treat leaf nodes and connections as a graph structure and apply a bread-first-search from boundary nodes until it reaches occupied nodes. All visited empty nodes during the search are additionally marked as exterior nodes. We loop over each leaf occupied nodes and check whether any of its neighbors are marked as the exterior. We extract faces shared by occupied and exterior nodes as two triangles and collect all extracted triangles to form our new mesh. Examples of extracted faces are shown in Figure 3 (b) and (c).

During manifold extraction, there are two corner cases that prevent our extracted mesh from being a manifold. First, non-manifold edges appear when exactly two diagonal voxels are occupied of the edge's four incident voxels, as shown in Figure 4(a). We split the edge into two in order to disconnect the voxels. In our implementation, we construct a standard half-edge structure where non-manifold edges are duplicated as four half-edges where each pair of half-edges belonging to the same voxel are marked as twins. For example, half-edges for face f_1 and f_2 are paired as a twin, f_3 and f_4 are paired as another twin in Figure 4(a). Second, a vertex could be shared by several groups of locally connected voxels, as shown in Figure 4(b). We identify each separate group by traversing and collecting half-edges in the counter-clockwise order, split the vertex, and assign it to each group (green arrows in Figure 4(b)).

After processing the above cases, we can guarantee that our extracted mesh is a perfect watertight manifold.

3.2 Manifold Optimization Formulation

We aim at optimizing \mathcal{M}_t and stick it to the reference mesh \mathcal{M}_r to remove the voxel-shape artifacts. The energy of any vertex k in the output mesh is defined as the squared distance to the nearest point

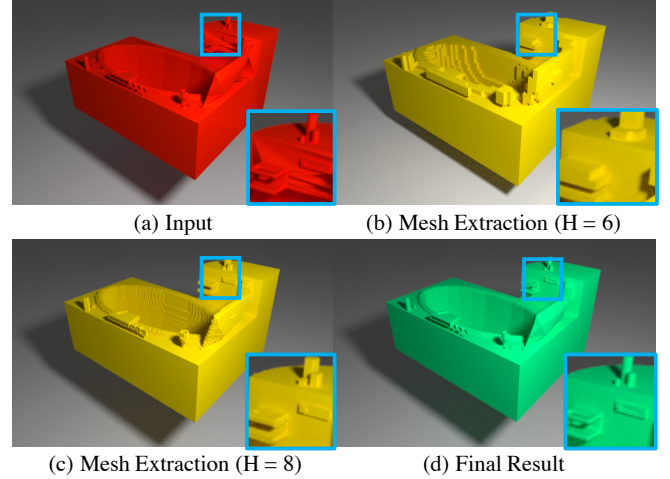


Fig. 3. Mesh extraction example. The input is in (a) where problematic face orientation causes rendering artifacts in the zoomed-in planar region. (b) and (c) are manifold meshes extracted using our method at different resolutions. (d) is our final result based on (c) followed by an optimization step (Section 3.2-3.4), which is close to (a) but without less rendering artifacts.

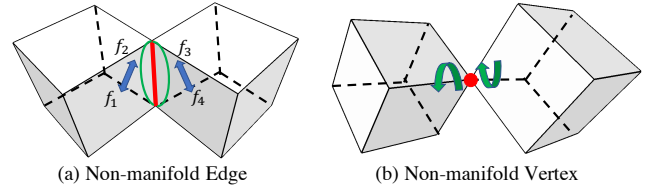


Fig. 4. Non-manifold edge and vertex examples. (a) Non-manifold edges (red) appears when two diagonal voxels are occupied among the edge's four incident voxels. (b) Non-manifold vertex is shared by more than one group of connected triangles.

\mathbf{p}_k in the reference mesh:

$$E_D(\mathbf{v}_k) = \min_{\mathbf{p}_k \in \mathcal{M}_r} \|\mathbf{v}_k - \mathbf{p}_k\|_2^2, \quad (1)$$

where \mathbf{v}_k is a *variable* representing the coordinate of vertex k in the output.

In order to guarantee that the orientation of all the triangles is consistent with their neighborhood so that there is no flipping triangles, we associate each vertex k with an *variable* $\mathbf{n}_k \in \mathbb{R}^3$ representing its local orientation, i.e., the normal direction of that vertex. This leads to constraints that for each triangle Δabc in the output, we have

$$\mathbf{n}_{abc} \cdot \mathbf{n}_k > 0 \quad \forall k \in \{a, b, c\}. \quad (2)$$

Here, \mathbf{n}_{abc} denotes the face normal of Δabc on the output mesh computed from vertex position \mathbf{v}_k (we denote face normal with 3 characters and vertex normals with 1 character in subscript). Equation 2 can be interpreted as the introduction of a vertex normal as a proxy to coordinate face orientations surrounding each vertex. To best represent its local orientation, we require vertex normals \mathbf{n}_k to

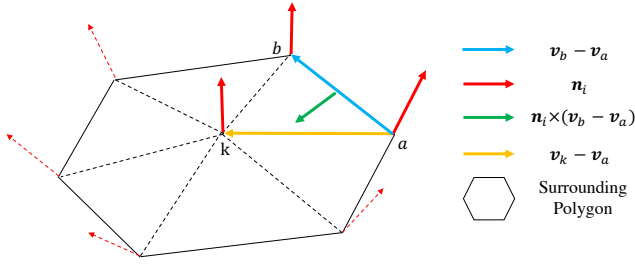


Fig. 5. Vertex k are kept inside its surrounding polygon projected to local tangent planes specified by vertex normal of i which equals or is adjacent to k .

be as close to the interpolated normal direction $\tilde{\mathbf{n}}_k$ of vertex k :

$$E_N(\mathbf{n}_k, \tilde{\mathbf{n}}_k) = \|\mathbf{n}_k - \tilde{\mathbf{n}}_k\|_2^2 \quad (3)$$

The interpolated normal direction $\tilde{\mathbf{n}}_k$ is computed by averaging \mathbf{n}_{abc} for all the triangles that are adjacent to vertex k . Our problem formulation is summarized in the following optimization problem:

$$\begin{aligned} & \underset{\{\mathbf{v}_k\}, \{\mathbf{n}_k\}}{\text{minimize}} && \sum_{k=1}^{|\mathcal{V}_t|} E_D(\mathbf{v}_k) + E_N(\mathbf{n}_k, \tilde{\mathbf{n}}_k) \\ & \text{subject to} && \mathbf{n}_{abc} \doteq (\mathbf{v}_b - \mathbf{v}_a) \times (\mathbf{v}_c - \mathbf{v}_a) \\ & && \tilde{\mathbf{n}}_k \doteq \frac{\sum_{\Delta abc \in \mathcal{N}_k} \mathbf{n}_{abc}}{\|\sum_{\Delta abc \in \mathcal{N}_k} \mathbf{n}_{abc}\|_2} \\ & && \mathbf{n}_{abc} \cdot \mathbf{n}_k > 0 \quad \Delta abc \in \mathcal{F}_t, k \in \{a, b, c\} \\ & && \|\mathbf{n}_k\|_2 = 1 \quad 1 \leq k \leq |\mathcal{V}_t|. \end{aligned} \quad (4)$$

Here, \doteq is the symbol of “defined as” and \mathcal{N}_k is the set of all triangles that are adjacent to vertex k .

3.3 Solving the optimization

Equation 4 is non-trivial to solve since it is a large, non-convex system with complex constraints. However, we observe the following favored properties in the problem. First, by initializing vertex positions \mathbf{v}_k with the manifold generated by the method in Section 3.1 and \mathbf{n}_k as $\tilde{\mathbf{n}}_k$, all constraints in Equation 4 are satisfied because the initial mesh is inversion-free. Second, this initialization is close to the optimal solution since the extracted mesh is not far from the reference mesh. This suggests that a proper local iterative method is promising to obtain decent results. Third, we notice that by fixing all other variables and solve for a single one, the original problem can be converted to a convex optimization problem. Therefore, we propose to apply a Gauss-Seidel method that iteratively updates the position and normal for each vertex fixing all other variables, where each update is a convex optimization.

Vertex Update. To update the position of k -th vertex, we find its nearest position \mathbf{p}_k in the reference mesh \mathcal{M}_r , which can be efficiently computed by pre-storing an AABB tree [Bergin 1997] for \mathcal{M}_r ³. We aim at moving \mathbf{v}_k to \mathbf{p}_k maintaining all constraints. Since

³https://github.com/libigl/libigl/blob/master/include/igl/point_mesh_squared_distance.cpp

all face normals near vertex k are changed during the vertex movement, consistency constraints can be violated between face normals for any of these triangles and their vertices’ normals. Therefore, a subproblem can be extracted from Equation 4 as Equation 5. We set $\varepsilon_v = 10^{-5}$ as a positive threshold

$$\begin{aligned} & \underset{\mathbf{v}_k}{\text{minimize}} && \|\mathbf{v}_k - \mathbf{p}_k\|_2^2 \\ & \text{subject to} && \mathbf{n}_{kab} \cdot \mathbf{n}_i \geq \varepsilon_v \\ & && \forall \Delta_{kab} \in \mathcal{F}_t, i \in \{k, a, b\} \end{aligned} \quad (5)$$

Here, $\mathbf{n}_{kab} = (\mathbf{v}_a - \mathbf{v}_k) \times (\mathbf{v}_b - \mathbf{v}_k)$ is linear with respect to \mathbf{v}_k as $\mathbf{v}_k \times \mathbf{v}_k = \mathbf{0}$. As shown in Figure 5, this linear relationship is also geometrically meaningful: we require vertex \mathbf{v}_k to sit inside its surrounding 2D polygon by projecting the neighborhoods to the local tangent planes specified by any vertex normal which is or is adjacent to k . Therefore, Equation 5 is a convex problem with quadratic energy and linear constraints. We solve it with the simplex algorithm [Vanderbei et al. 2015]: Initially, we set the target position as \mathbf{p}_k . First, we move \mathbf{v}_k towards the target until it reaches certain boundary constraint. Second, we project the target position to set of activated boundary constraints and go back to the first step. The algorithm terminates when we reach the target position or trapped into a corner when the rank of boundary constraints is 3. Since each constraint is becoming the boundary for at most once, the time complexity is linear to the number of constraints. The amortized time complexity over the whole mesh for vertex updates is $O(|\mathcal{F}_t|)$.

Normal Update. To update k -th vertex normal \mathbf{v}_k , we first compute the target normal $\tilde{\mathbf{n}}_k$ by interpolating the current neighboring face normals. We extract the related energy term and constraints from Equation 4 and solve Equation 6, where we set $\varepsilon_n = 10^{-2}$.

$$\begin{aligned} & \underset{\mathbf{n}_k}{\text{minimize}} && \|\mathbf{n}_k - \tilde{\mathbf{n}}_k\|_2^2 \\ & \text{subject to} && \mathbf{n}_{kab} \cdot \mathbf{n}_k \geq \varepsilon_n \quad \Delta_{kab} \in \mathcal{F}_t \\ & && \|\mathbf{n}_k\|_2 = 1 \end{aligned} \quad (6)$$

Although the unit-vector constraint $\|\mathbf{n}_k\|_2 = 1$ makes this problem non-convex, we can relax the problem by removing it and solve a convex problem with solution denoted as $\hat{\mathbf{n}}_k$. Note that \mathbf{n}_{kab} are computed from vertex positions, which are considered as constants in the normal update process. Then, we derive Theorem 3.1.

THEOREM 3.1. *The global optimal solution of Equation 6 is identical to $\frac{\hat{\mathbf{n}}_k}{\|\hat{\mathbf{n}}_k\|}$, where $\hat{\mathbf{n}}_k$ is the global optimal solution of the same problem but removing the constraint $\|\mathbf{n}_k\|_2 = 1$.*

PROOF. If $\tilde{\mathbf{n}}_k$ satisfies all constraints, the theorem is valid because the energy is zero.

Otherwise, $\tilde{\mathbf{n}}_k$ is outside the volume specified by the constraints as a polygon shown in Figure 6 (blue lines). $\hat{\mathbf{n}}_k$ is the projection of $\tilde{\mathbf{n}}_k$ to the boundary of the polygon (green spot inside the sphere) and $\frac{\hat{\mathbf{n}}_k}{\|\hat{\mathbf{n}}_k\|}$ is shown as the green spot at the sphere boundary. For any other feasible solution \mathbf{n}_k , we can project $\tilde{\mathbf{n}}_k$ to line $\langle \mathbf{O}, \mathbf{n}_k \rangle$ as \mathbf{a} . Since $\hat{\mathbf{n}}_k$ is the optimal solution without unit-vector constraints, it is closer to $\tilde{\mathbf{n}}_k$ than \mathbf{a} . Therefore, the angle between $\hat{\mathbf{n}}_k$ and $\tilde{\mathbf{n}}_k$ is smaller than that between \mathbf{a} and $\tilde{\mathbf{n}}_k$. Therefore, $\frac{\hat{\mathbf{n}}_k}{\|\hat{\mathbf{n}}_k\|}$ is closer to any other solution \mathbf{n}_k , and is the global optimal for Equation 6. \square

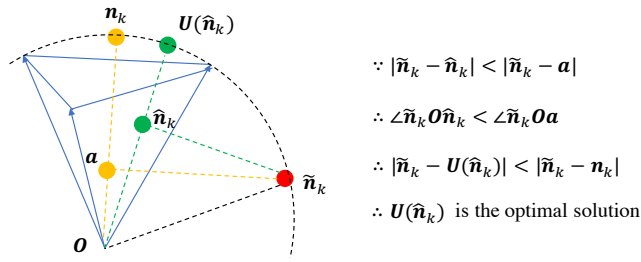


Fig. 6. Illustration of optimal normal solution for Equation 6. Feasible solutions sit on the sphere surface inside the 3D polygon specified by linear constraints. Optimal solution is the normalization of the point $\hat{\mathbf{n}}_k$ inside the polygon that is closest to $\tilde{\mathbf{n}}_k$.

According to Theorem 3.1, we update vertex normal with $\mathbf{n}_k \leftarrow \frac{\hat{\mathbf{n}}_k}{\|\hat{\mathbf{n}}_k\|}$ as the optimal solution. Note that $\hat{\mathbf{n}}_k$ can be solved using the same algorithm applied to Equation 5. Therefore, the time complexity for updating all vertex normals in one pass is also $O(|\mathcal{V}_t|)$.

Gauss-Seidel Update. We maintain an active vertex list before each pass of vertex and normal update. During each pass, we loop over the vertex list in the decreasing order of $E_D(\mathbf{v}_k)$, update the vertex position by solving Equation 5 and vertex normal by solving Equation 6. If a vertex is updated, the vertex and its adjacent vertices are inserted into the active vertex list for the next pass. We terminate the algorithm when no more vertex is updated. Initially, the active vertex list contains all vertex in \mathcal{V}_t . In practice, we find that the total number of vertex updates is at the scale of $O(|\mathcal{F}_t|)$ with a constant coefficient smaller than 10. Therefore, our algorithm is efficient for handling meshes on a large scale.

3.4 Sharp Preservation

Although \mathcal{M}_t is stitched to the reference mesh \mathcal{M}_r during optimization at mesh vertices \mathcal{V}_t , there is no guarantee that edges also perfectly sit in \mathcal{M}_r . This leads to the failure of sharp feature preservation as shown in Figure 7(a). However, it also gives us intuition to detect problematic edges: an edge breaks the sharp feature if its midpoint is not close enough (10^{-3} of voxel size in our implementation) to \mathcal{M}_r . Therefore, we cut such an edge at its midpoint and move it to the sharp feature line in \mathcal{M}_r using the same vertex and normal update in Section 3.3. We first detect all edges that need to be cut, and subdivide the triangles depending on the number of edges to cut as shown in Figure 8, where we aim to move blue vertices to sharp edges and the red vertex is to the sharp corner. For an edge with blue vertex, the target position is the projection of the midpoint to the intersection line of planes in the reference mesh where the edge endpoints sit in. For the triangle with the red vertex, the corner is determined by intersecting three planes of the reference mesh where the triangle vertices sit in. Figure 7 demonstrates the before and after using sharp preserving processing.

4 RESULTS

We evaluate the performance of our algorithm based on several criteria related to correctness, efficiency and accuracy. We compare

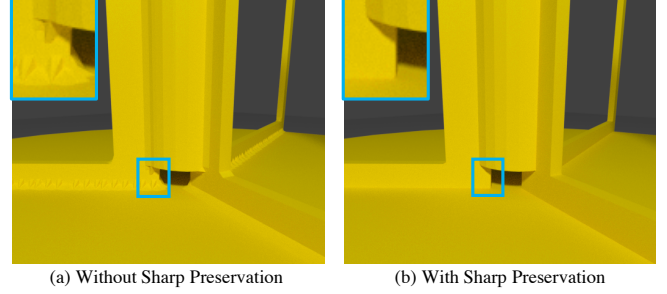


Fig. 7. Sharp feature preservation example. By projecting newly added vertices to sharp locations, sharp features can be preserved.

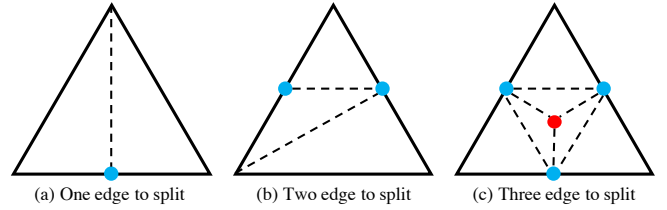


Fig. 8. We subdivide a triangle based on the number of edges to cut. Blue vertices are moved to sharp edges and red vertices are moved to sharp corners.

with several state-of-the-art methods including “MeshFix” [Attene 2010], “TetWild” [Hu et al. 2018], “PolyMender” [Ju 2004], “OuterHull” [Attene 2017, 2018], “Manifold” [Huang et al. 2018a], and “Visual” [Chu et al. 2019]. We massively evaluate proposed methods for all models from the ModelNet10 dataset [Wu et al. 2015]. Visual results are shown in Figure 10.

Correctness. We evaluate whether a result is topologically an oriented watertight 2-manifold by checking the existence of boundary edges, non-manifold edges (NM Edges), non-manifold vertices (NM Vertices), and triangle inversions based on our proposed criterion. Table 1 shows the comparison. As a result, MeshFix [Attene 2010], TetWild [Hu et al. 2018] and Visual [Chu et al. 2019] fail to process hundreds of shapes for ModelNet10. PolyMender [Ju 2004], Manifold [Huang et al. 2018a] and our method are robust to process all shapes. We consider OuterHull [Attene 2017, 2018] as almost robust since it fails to process less than 1% among all shapes. Among all successfully-processed models, 38 from OuterHull have non-manifold edges or vertices. Although both Manifold [Huang et al. 2018a] and Visual [Chu et al. 2019] are free from non-manifold edges, Manifold [Huang et al. 2018a] yields non-manifold vertices and Visual [Chu et al. 2019] yields boundary edges. Our method robustly handles these problems correctly and generates results that capture geometry details in the input as shown in Figure 10.

Efficiency. We report the processing time of different methods on different input shapes. As shown in Table 2. PolyMender [Ju 2004], Manifold [Huang et al. 2018a], and our method can be considered as efficient since these methods can process object-level models

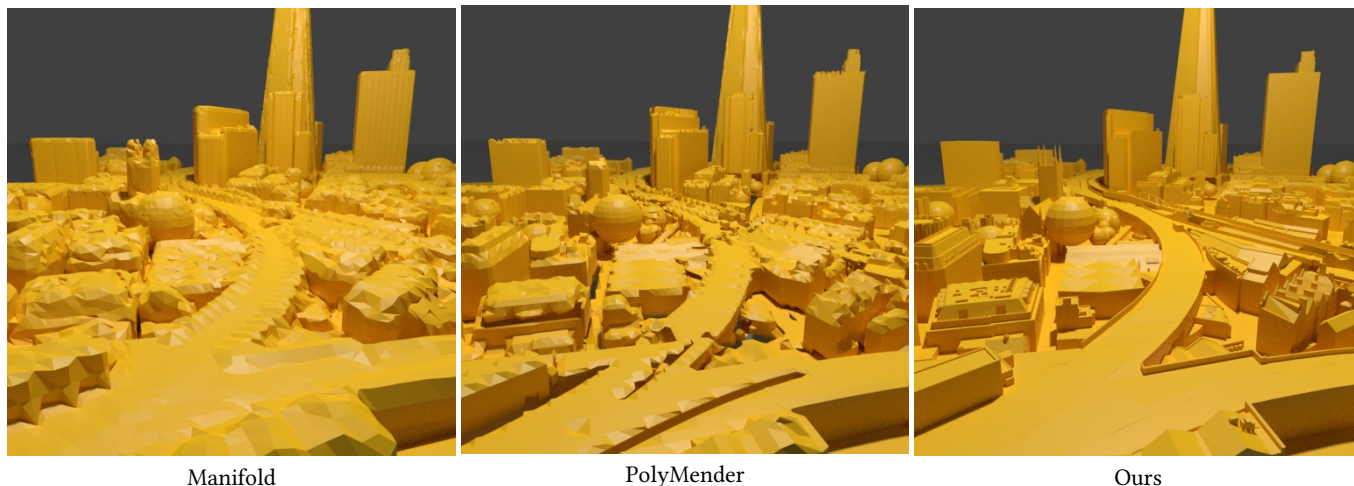


Fig. 9. City manifold results successfully processed by different methods. Our method is the only one that preserves details of the city.

	Boundary	NM Edges	NM Vertices	Failure
MeshFix	0	0	0	2416
TetWild	0	2465	2545	1421
PolyMender	0	0	0	0
OuterHull	38	0	38	37
Manifold	0	0	210	0
Visual	3250	0	3259	406
Ours	0	0	0	0

Table 1. Number of results violating certain criteria in ModelNet10 among 4899 models.

	Bathtub	Gargoyle	Rampant	HoliCity
MeshFix	68.8	2.0	2.4	Fail
TetWild	89.7	733	238	Fail
PolyMender	2.6	4.3	2.3	19.7
OuterHull	65.5	5.2	5.7	Fail
Manifold	2.4	3.3	4.2	28.7
Visual	Fail	20.2	39.5	Fail
Ours	3.7	5.2	4.6	271

Table 2. Time consumed for different methods to process different input meshes.

(Bathtub, Gargoyle, and Rampant) in less than 10 seconds. Additionally, only these three methods can handle the city-scale CAD model in our experiment. The city results from these methods are visualized in Figure 9. Among these methods, ours is the only one that preserves details of the entire city.

Accuracy. We measure the remeshing accuracy by the maximum and mean distance between extracted vertices to the reference mesh, denoted as T2R-max and T2R-mean. In order to demonstrate the capability of zero-volume structure preservation, we additionally evaluate the coverage by measuring the maximum and mean distance

	T2R-max	T2R-mean	R2T-max	R2T-mean
MeshFix	0	0	1.9×10^{-1}	5.0×10^{-2}
TetWild	2.7×10^{-2}	9.3×10^{-4}	2.1×10^{-1}	6.3×10^{-2}
PolyMender	3.8×10^{-2}	2.2×10^{-3}	6.3×10^{-2}	6.2×10^{-3}
OuterHull	4.6×10^{-3}	3.8×10^{-4}	4.5×10^{-3}	3.3×10^{-4}
Manifold	1.2×10^{-2}	7.6×10^{-3}	3.1×10^{-2}	5.4×10^{-3}
Visual	3.2×10^{-3}	1.1×10^{-4}	8.9×10^{-3}	1.9×10^{-4}
Ours	1.2×10^{-3}	8.9×10^{-6}	3.3×10^{-3}	7.3×10^{-6}

Table 3. Fitting quality between the exterior regions of input mesh and results from different methods.

from exterior regions of the reference mesh to the reconstructed mesh, denoted as R2T-max and R2T-mean. We compute the average of these terms for all processed models with different methods, and report scores in Table 3. For this experiment, we normalize each object with a uniform scale so that the maximum axis length of its bounding box is two units. Although direct comparison is not valid since different methods successfully handle different sets of objects, we can draw some conclusions from the scale of the errors. MeshFix [Attene 2010], TetWild [Hu et al. 2018] and PolyMender [Ju 2004] cannot preserve the original geometry well where maximum geometry errors is at the scale of 10^{-2} . Manifold [Huang et al. 2018a] preserves better geometry but tends to produce thicker geometry and cannot preserve sharp features. OuterHull [Attene 2017, 2018], Visual [Chu et al. 2019] and our method nearly preserve all geometry details, and our method achieves smallest fitting error. The above discussed problems are reflected in Figure 10. Among all successfully generated models, OuterHull [Attene 2017, 2018], Visual [Chu et al. 2019] and our method can produce results quite similar to the input CAD models.

Remeshing Triangles. In Figure 11, we visualize various manifold models that we produce in ModelNet10 with faithful geometry detail preservation. In these examples, we are able to preserve sharp

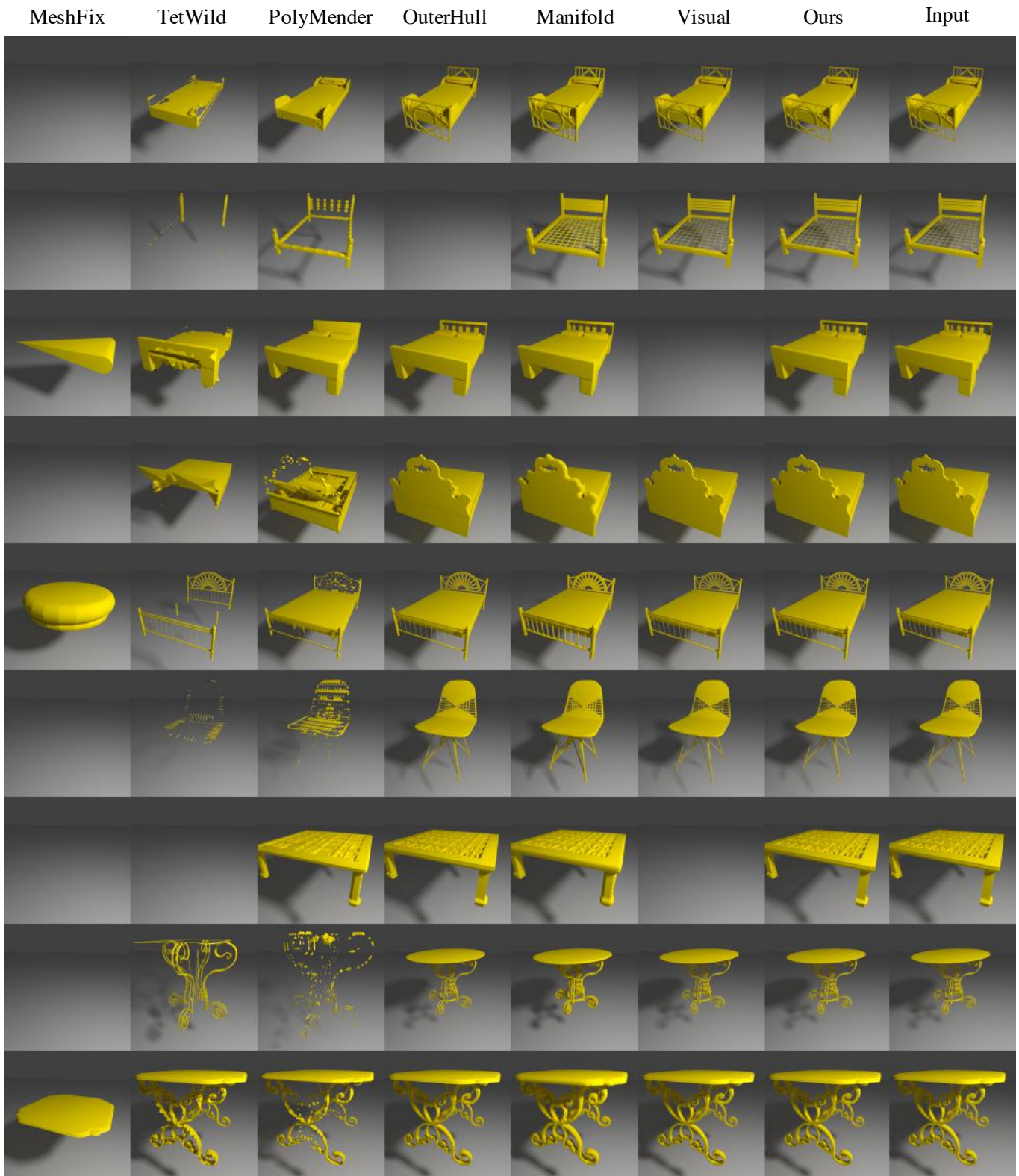


Fig. 10. Visual results generated from different methods on ModelNet10 [Wu et al. 2015].



Fig. 11. Visualization of ModelNet10 manifold result generated by our method.



Fig. 12. We successfully create manifold for models with self-intersections, and can deal with möbius strip and organic shapes.

features, zero-volume structures and tiny holes while guarantee watertight manifold topology. Additionally, we successfully create manifold for models with self-intersections, and can deal with möbius strip or organic shapes, as shown in Figure 12.

Remeshing Scan. We slightly change our algorithm to enable surface reconstruction from scanning data. Our input is aligned multi-view depth images and our output is a reconstructed triangle mesh. We simply extract point clouds from all range images, merge them together in the world coordinate system, and run our algorithm to obtain the reconstruction, where the only difference is to compute E_D based on nearest point-to-point distance instead of point-to-mesh distance. We compare our algorithm with commonly used Poisson surface reconstruction [Kazhdan et al. 2006] and TSDF reconstruction [Curless and Levoy 1996]. By Poisson reconstruction, we compute the point normals of the extracted point cloud based on jet fitting and apply the Poisson surface reconstruction implemented in CGAL. Table 4 reports the chamfer distances in both ways between the ground truth and results generated from different methods. Visualization of surface reconstruction is shown in Figure 13. TSDF reconstruction suffers from inaccurate per-frame distance field estimation, which causes relatively large errors at the edges (Figure 13. Poisson reconstruction is suffering from large

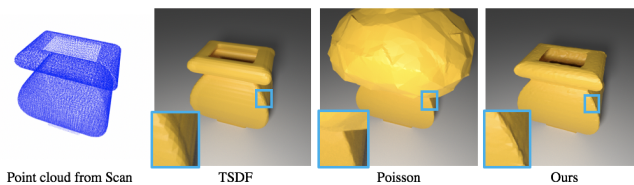


Fig. 13. Surface reconstruction from range images. Our method provides more accurate reconstruction and is robust to large holes in scans.

	Poisson	TSDF	Ours
Point-to-Scan	5.44×10^{-2}	2.71×10^{-2}	2.56×10^{-2}
Scan-to-Point	23.6×10^{-2}	8.73×10^{-2}	1.48×10^{-2}

Table 4. Chamfer distance between the ground truth point cloud and the surface reconstruction result.

holes where there is no observed data. Distance field at these regions is only regularized by inaccurate modeling of boundary condition and usually cause the wrong reconstruction. These problems cause significant larger errors compared with our methods by measuring the distance from the scan to the point cloud. Our method provides more accurate reconstruction and is robust to large holes in scans.

5 CONCLUSION

We present a robust, scalable, and accurate surface reconstruction algorithm that guarantees to provide watertight manifold for triangle soups. We specifically deal with challenges of orientation ambiguity and thin structures commonly existing in available 3D data. We use a volumetric representation to extract surfaces between exterior and occupied voxels and thereby remove orientation ambiguity.

In the future, there are several things that can be considered to further improve manifold remeshing. First, now we fix a hole if its size is smaller than a voxel size. However, the artist created CAD models could have big holes. It is interesting to explore semantic information in order to decide whether to fix the holes. Second, our method is not designed for noisy scanning data. It is a promising direction to combine our method jointly with denoising for better surface reconstruction.

REFERENCES

- Aseem Agarwala. 2007. Efficient gradient-domain compositing using quadtrees. *ACM Transactions on Graphics (TOG)* 26, 3 (2007), 94–es.
- Marco Attene. 2010. A lightweight approach to repairing digitized polygon meshes. *The visual computer* 26, 11 (2010), 1393–1406.
- Marco Attene. 2014. Direct repair of self-intersecting meshes. *Graphical Models* 76, 6 (2014), 658–668.
- Marco Attene. 2017. ImatiSTL-fast and reliable mesh processing with a hybrid kernel. In *Transactions on Computational Science XXIX*. Springer, 86–96.
- Marco Attene. 2018. As-exact-as-possible repair of unprintable STL files. *Rapid Prototyping Journal* (2018).
- Marco Attene, Marcel Campen, and Leif Kobbelt. 2013. Polygon mesh repairing: An application perspective. *ACM Computing Surveys (CSUR)* 45, 2 (2013), 1–33.
- David Baraff and Andrew Witkin. 1998. Large steps in cloth simulation. In *Proceedings of the 25th annual conference on Computer graphics and interactive techniques*. 43–54.
- Gino van den Bergen. 1997. Efficient collision detection of complex deformable models using AABB trees. *Journal of graphics tools* 2, 4 (1997), 1–13.
- Paul J Besl and Neil D McKay. 1992. Method for registration of 3-D shapes. , 586–606 pages.

- Jean-Daniel Boissonnat. 1984. Geometric structures for three-dimensional shape representation. *ACM Transactions on Graphics (TOG)* 3, 4 (1984), 266–286.
- Brent Burley and Dylan Lacey. 2008. Ptex: Per-face texture mapping for production rendering. In *Computer Graphics Forum*, Vol. 27. Wiley Online Library, 1155–1164.
- Fatih Calakli and Gabriel Taubin. 2011. SSD: Smooth signed distance surface reconstruction. In *Computer Graphics Forum*, Vol. 30. Wiley Online Library, 1993–2002.
- Angel X Chang, Thomas Funkhouser, Leonidas Guibas, Pat Hanrahan, Qixing Huang, Zimo Li, Silvio Savarese, Manolis Savva, Shuran Song, Hao Su, et al. 2015. Shapenet: An information-rich 3d model repository. *arXiv preprint arXiv:1512.03012* (2015).
- Yang Chen and Gérard G Medioni. 1992. Object modeling by registration of multiple range images. *Image Vision Comput.* 10, 3 (1992), 145–155.
- Evgeni Chernyaev. 1995. *Marching cubes 33: Construction of topologically correct isosurfaces*. Technical Report.
- L Paul Chew. 1989. Constrained delaunay triangulations. *Algorithmica* 4, 1-4 (1989), 97–108.
- Lei Chu, Hao Pan, Yang Liu, and Wenping Wang. 2019. Repairing man-made meshes via visual driven global optimization with minimum intrusion. *ACM Transactions on Graphics (TOG)* 38, 6 (2019), 158.
- Brian Curless and Marc Levoy. 1996. A volumetric method for building complex models from range images. In *Proceedings of the 23rd annual conference on Computer graphics and interactive techniques*. 303–312.
- Yago Diez, Ferran Roure, Xavier Lladó, and Joaquim Salvi. 2015. A qualitative review on 3D coarse registration methods. *ACM Computing Surveys (CSUR)* 47, 3 (2015), 1–36.
- Akio Doi and Akio Koide. 1991. An efficient method of triangulating equi-valued surfaces by using tetrahedral cells. *IEICE TRANSACTIONS on Information and Systems* 74, 1 (1991), 214–224.
- Martin J Düst. 1988. Re: Additional reference to "marching cubes". *ACM SIGGRAPH Computer Graphics* 22, 5 (1988), 243.
- Natasha Gelfand and Leonidas J Guibas. 2004. Shape segmentation using local slippage analysis. In *Proceedings of the 2004 Eurographics/ACM SIGGRAPH symposium on Geometry processing*. 214–223.
- André Guéziec, Gabriel Taubin, Francis Lazarus, and B Hom. 2001. Cutting and stitching: Converting sets of polygons to manifold surfaces. *IEEE Transactions on Visualization and Computer Graphics* 7, 2 (2001), 136–151.
- Alexander Hornung and Leif Kobbelt. 2006. Robust reconstruction of watertight 3 d models from non-uniformly sampled point clouds without normal information. In *Symposium on geometry processing*. Citeseer, 41–50.
- Y Hu, Q Zhou, X Gao, A Jacobson, D Zorin, and D Panozzo. 2018. Tetwild-tetrahedral meshing in the wild. *ACM Transactions on Graphics (to appear)* (2018).
- Jingwei Huang, Hao Su, and Leonidas Guibas. 2018a. Robust watertight manifold surface generation method for shapenet models. *arXiv preprint arXiv:1802.01698* (2018).
- Jingwei Huang, Haotian Zhang, Li Yi, Thomas Funkhouser, Matthias Nießner, and Leonidas J Guibas. 2019. TextureNet: Consistent local parametrizations for learning from high-resolution signals on meshes. In *Proceedings of the IEEE Conference on Computer Vision and Pattern Recognition*. 4440–4449.
- Jingwei Huang, Yichao Zhou, Matthias Niessner, Jonathan Richard Shewchuk, and Leonidas J Guibas. 2018b. QuadriFlow: A scalable and robust method for quadrangulation. In *Computer Graphics Forum*, Vol. 37. Wiley Online Library, 147–160.
- Wenzel Jakob, Marco Tarini, Daniele Panozzo, and Olga Sorkine-Hornung. 2015. Instant field-aligned meshes. *ACM Trans. Graph.* 34, 6 (2015), 189–1.
- Tao Ju. 2004. Robust repair of polygonal models. *ACM Transactions on Graphics (TOG)* 23, 3 (2004), 888–895.
- Michael Kazhdan, Matthew Bolitho, and Hugues Hoppe. 2006. Poisson surface reconstruction. In *Proceedings of the fourth Eurographics symposium on Geometry processing*, Vol. 7.
- Michael Kazhdan and Hugues Hoppe. 2013. Screened poisson surface reconstruction. *ACM Transactions on Graphics (ToG)* 32, 3 (2013), 1–13.
- Yong Se Kim. 1992. Recognition of form features using convex decomposition. *Computer-Aided Design* 24, 9 (1992), 461–476.
- Hao Li, Robert W Sumner, and Mark Pauly. 2008. Global correspondence optimization for non-rigid registration of depth scans. In *Computer graphics forum*, Vol. 27. Wiley Online Library, 1421–1430.
- William E Lorensen and Harvey E Cline. 1987. Marching cubes: A high resolution 3D surface construction algorithm. *ACM siggraph computer graphics* 21, 4 (1987), 163–169.
- Jonathan Masci, Davide Boscaini, Michael Bronstein, and Pierre Vandergheynst. 2015. Geodesic convolutional neural networks on riemannian manifolds. In *Proceedings of the IEEE international conference on computer vision workshops*. 37–45.
- TM Murali and Thomas A Funkhouser. 1997. Consistent solid and boundary representations from arbitrary polygonal data. In *Proceedings of the 1997 symposium on Interactive 3D graphics*. 155–f.
- Richard A Newcombe, Dieter Fox, and Steven M Seitz. 2015. Dynamicfusion: Reconstruction and tracking of non-rigid scenes in real-time. In *Proceedings of the IEEE conference on computer vision and pattern recognition*. 343–352.
- Richard A Newcombe, Shahram Izadi, Otmar Hilliges, David Molyneaux, David Kim, Andrew J Davison, Pushmeet Kohi, Jamie Shotton, Steve Hodges, and Andrew Fitzgibbon. 2011. KinectFusion: Real-time dense surface mapping and tracking. In *2011 10th IEEE International Symposium on Mixed and Augmented Reality*. IEEE, 127–136.
- Fakir S. Nooruddin and Greg Turk. 2003. Simplification and repair of polygonal models using volumetric techniques. *IEEE Transactions on Visualization and Computer Graphics* 9, 2 (2003), 191–205.
- Roi Poranne, Marco Tarini, Sandro Huber, Daniele Panozzo, and Olga Sorkine-Hornung. 2017. Autocuts: simultaneous distortion and cut optimization for UV mapping. *ACM Transactions on Graphics (TOG)* 36, 6 (2017), 1–11.
- Laurent Rineau and Mariette Yvinec. 2007. A generic software design for Delaunay refinement meshing. *Computational Geometry* 38, 1-2 (2007), 100–110.
- Jarek Rossignac and David Cardoze. 1999. Matchmaker: Manifold Breps for non-manifold r-sets. In *Proceedings of the fifth ACM symposium on Solid modeling and applications*. 31–41.
- Szymon Rusinkiewicz and Marc Levoy. 2001. Efficient variants of the ICP algorithm. In *Proceedings Third International Conference on 3-D Digital Imaging and Modeling*. IEEE, 145–152.
- Jonathan Richard Shewchuk. 2002. Delaunay refinement algorithms for triangular mesh generation. *Computational geometry* 22, 1-3 (2002), 21–74.
- Olga Sorkine and Marc Alexa. 2007. As-rigid-as-possible surface modeling. In *Symposium on Geometry processing*, Vol. 4. 109–116.
- Robert W Sumner, Johannes Schmid, and Mark Pauly. 2007. Embedded deformation for shape manipulation. In *ACM SIGGRAPH 2007 papers*. 80–es.
- Mikaela Angelina Uy, Jingwei Huang, Minhyuk Sung, Tolga Birdal, and Leonidas Guibas. 2020. Deformation-Aware 3D Model Embedding and Retrieval. *arXiv preprint arXiv:2004.01228* (2020).
- Robert J Vanderbei et al. 2015. *Linear programming*. Springer.
- Xunlei Wu, Michael S Downes, Tolga Goktekin, and Frank Tendick. 2001. Adaptive nonlinear finite elements for deformable body simulation using dynamic progressive meshes. In *Computer Graphics Forum*, Vol. 20. Wiley Online Library, 349–358.
- Zhirong Wu, Shuran Song, Aditya Khosla, Fisher Yu, Linguang Zhang, Xiaoou Tang, and Jianxiong Xiao. 2015. 3D ShapeNets: A deep representation for volumetric shapes. In *Proceedings of the IEEE conference on computer vision and pattern recognition*. 1912–1920.
- Olgierd Cecil Zienkiewicz, Robert Leroy Taylor, Perumal Nithiarasu, and JZ Zhu. 1977. *The finite element method*. Vol. 3. McGraw-hill London.

APPENDIX

A BUILD OCTREE

Detailed algorithm for building initial octree from the reference mesh is shown in Algorithm 1, where the initial call sets $\mathcal{F} = \mathcal{F}_r$ and depth as 0.

B BUILD OCTREE CONNECTIONS

We build internal connections in the octree recursively by calling ConnectOctree in Algorithm 2, where it recursively builds internal connections in the children and additionally build external connections between neighboring children in Algorithm 3.

ALGORITHM 1: ConstructVolume

Input: \mathcal{F} , Octree Node T , Current depth d , Target tree height H
Output: Constructed Octree T

```

1 if  $d = 0$  then
2    $T.\text{volume} \leftarrow [-1.1, 1.1]^3$ 
3    $T.\text{status} \leftarrow \text{Occupied}$ 
4    $T.\text{level} \leftarrow d$ 
5    $T.\text{children} \leftarrow \text{Node}[8]$ 
6 if  $d < H$  then
7   for  $i \leftarrow 1$  to 8 do
8      $C.\text{volume} \leftarrow i\text{-th half-cube of } T.\text{volume}$ 
9      $C.\text{status} \leftarrow \text{Empty}$ 
10     $C.\text{level} \leftarrow d + 1$ 
11     $\mathcal{F}_C \leftarrow \{f \mid f \in \mathcal{F} \text{ and intersects } C.\text{volume}\}$ 
12    if  $|\mathcal{F}_C| > 0$  then
13       $C.\text{status} \leftarrow \text{Occupied}$ 
14       $\text{ConstructVolume}(\mathcal{F}_C, C, d + 1, d^*)$ 
15     $T.\text{children}[i] = C$ 
16 return  $T$ 

```

ALGORITHM 2: ConnectOctree

Input: Octree Node T
Output: T with Connections

```

1 if  $d < H$  then
2   for  $i \leftarrow 1$  to 8 do
3      $\text{ConnectOctree}(T.\text{children}[i])$ 
4    $P_x \leftarrow \{(1, 2), (3, 4), (5, 6), (7, 8)\}$ 
5    $P_y \leftarrow \{(1, 3), (2, 4), (5, 7), (6, 8)\}$ 
6    $P_z \leftarrow \{(1, 5), (2, 6), (3, 7), (4, 8)\}$ 
7   for  $p \in P_x$  do
8      $\text{ConnectNodes}(T.\text{children}[p.x], T.\text{children}[p.y], 1)$ 
9   for  $p \in P_y$  do
10     $\text{ConnectNodes}(T.\text{children}[p.x], T.\text{children}[p.y], 2)$ 
11   for  $p \in P_z$  do
12     $\text{ConnectNodes}(T.\text{children}[p.x], T.\text{children}[p.y], 3)$ 
13 return  $T$ 

```

ALGORITHM 3: ConnectNodes

Input: Neighboring Node A and B , and connecting direction d
Output: A and B with connections

```

1 if Both  $A$  and  $B$  are leaves then
2    $\text{Add an edge between } A \text{ and } B.$ 
3 else
4    $I_A \leftarrow [[2, 4, 6, 8], [3, 4, 7, 8], [5, 6, 7, 8]]$ 
5    $I_B \leftarrow [[1, 3, 5, 7], [1, 2, 5, 6], [1, 2, 3, 4]]$ 
6   if  $A$  is leaf then
7      $N_A \leftarrow [A, A, A, A]$ 
8   else
9      $N_A \leftarrow A.\text{children}[I_A[d]]$ 
10  if  $A$  is leaf then
11     $N_B \leftarrow [B, B, B, B]$ 
12  else
13     $N_B \leftarrow B.\text{children}[I_B[d]]$ 
14  for  $i \leftarrow 1$  to 4 do
15     $\text{ConnectNodes}(N_A[i], N_B[i])$ 
16 return  $T$ 

```

C MORE RESULTS ON MODELNET10

We provide more manifold results generated by our method in the ModelNet10 dataset [Wu et al. 2015] in Figure 14 for each category.

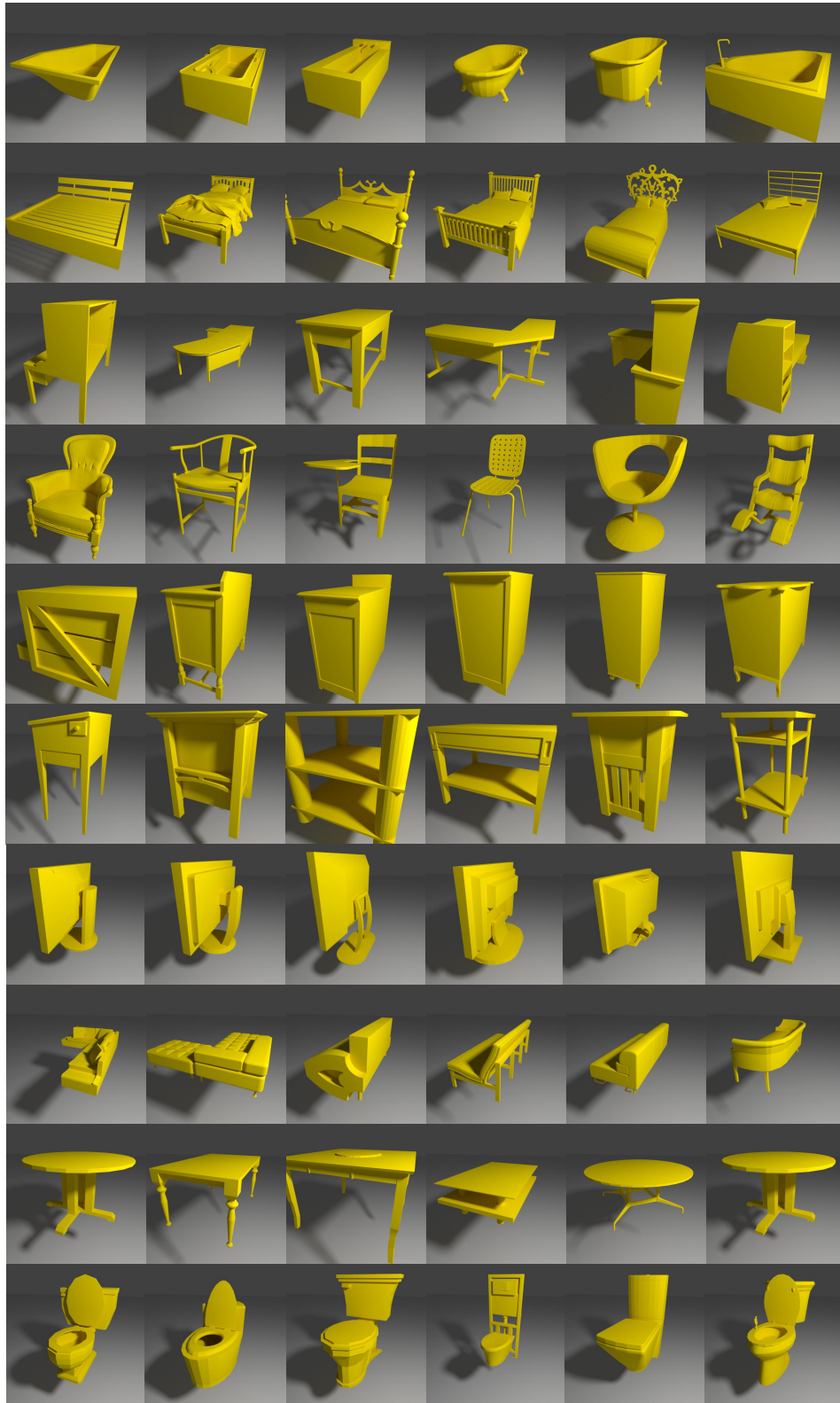


Fig. 14. Per-category ModelNet10 manifold results generated using our method.